Model Based Investigation of Anomalous Energy Transport in a Magnetically-Shielded Hall Thruster

IEPC-2024-411

Presented at the 38th International Electric Propulsion Conference, Toulouse, France
June 23-28, 2024

Declan G. Brick* and Benjamin A. Jorns†
University of Michigan, Ann Arbor, Michigan, 48109, United States of America

The electron energy transport in a multi-fluid Hall thruster model is modified to investigate effects on the plasma discharge of a Hall thruster. Direct measurements of the anomalous collision frequency are used to close the effects of non-classical momentum transport. This closure allows for variation of the energy equation to independently capture non-classical energy transport. Ion velocity and electron temperature profiles along centerline as well as global performance metrics of the discharge are employed to assess model performance. The non-classical electron heat flux perpendicular to magnetic field lines and wall energy losses are parametrically varied in attempt to match experimental measurement. It is found that a purely classical heat flux provides an improved agreement with measured plasma properties than when the anomalous collision frequency modifies the heat flux. An order of magnitude reduction of the energy losses to the wall and heat flux described by a classical Fourier's law correctly captures local plasma properties along channel centerline and match thruster discharge current. These results are discussed in the context of anomalous transport closures and boundary conditions in Hall thruster models.

I. Introduction

Despite the extensive flight heritage of Hall thrusters,[1–5] there are aspects of the physics of these devices that remain poorly understood.[6] In particular, the cross-field electron transport, the way in which bulk electron properties are transferred across magnetic field lines, is orders of magnitude higher than can be explained by classical effects. This poor understanding of the non-classical transport has precluded development of predictive Hall thruster models.

Due to the engineering and practical advantages afforded by such models, there has been extensive work in investigating ways to account for these non-classical effects. These efforts have primarily focused on approximating the non-classical effects as an effective "anomalous" collision frequency that enhances the cross-field electron mobility. Proposed "closure" models for this collision frequency have been based on Bohm-like diffusion,[7] wall collisions,[8,9] shear-suppression,[10–12] turbulence analogs,[13,14] wave driven,[15–17], dimensional analysis,[18] and data driven forms.[19] Despite this variety of attempts, none of these models have proved fully predictive when integrated into a self-consistent Hall thruster model.

While progress continues on these closures to capture the effects on momentum transport, the same level of scrutiny has not been applied to how non-classical effects could modify the electron energy transport in Hall thrusters. It is common practice to represent the heat flux using a Fourier formulation[20] while scaling the thermal conductivity using the anomalous collision frequency based on the momentum transport equations.[21–31] While this approach has been expedient in previous implementations, to our knowledge, there has yet to be rigorous demonstration that this approach to heat flux closure stems from first principles. To this point, recent numerical and experimental work has shown that using the anomalous collision frequency to enhance the heat flux in Hall thrusters in practice may not be appropriate. Numerical simulations using this form have been unable to simultaneously match experimental ion velocity and electron temperature

*PhD Candidate, Department of Aerospace Engineering, brickd@umich.edu
†Associate Professor, Department of Aerospace Engineering, and bjorns@umich.edu

measurements.[17] Experimentally-measured electron temperatures with non-invasive diagnostics have been shown to be a factor of two higher than previous probe and numerical values.[32,33] Combining the lack of theoretical justification with this inability of the closure to adequately describe measured electron energies, the need is apparent to revisit the treatment of anomalous energy transport in Hall thrusters.

To address this need, the goal of this work is to explore, through simulation, parametric modifications to the energy equation in a fluid-based Hall thruster model in an attempt to explain the experimentally observed temperatures, ion velocities, and performance metrics. The rest of the paper is organized as follows: In Sec. II we review anomalous transport in electron fluid models. In Sec. III we describe the Hall thruster and multi-fluid model used in this work. In Sec. IV we detail the modifications we will make to the energy equation to capture higher electron temperatures. In Sec. V we present our results and in Sec. VI discuss these results in the context of accounting for anomalous transport in the electron energy equation.

II. Fluid Theory of Electron Transport in Hall Thrusters

In this section, we first describe the steps of Hall thruster operation. We then present how the bulk electron momentum transport framework is modified to account for non-classical effects. We then discuss how the non-classical terms impact the energy transport and how they have been specified historically. Finally, we provide a high-level overview of the electron energy boundary conditions.

A. Principle of Operation

Figure 1 shows an image of Hall thruster with a canonical radial magnetic and axial electric field topology along with a cutaway view of the main components of the thruster. The four main thruster components are a thermionically emitting cathode, anode, discharge channel, and magnets. The anode and cathode form the operating circuit of the thruster to set up the axial electric field. The discharge channel is where the majority of the electron confinement, ionization, and ion acceleration occurs. The radial magnetic field is provided by either permanent magnets or electromagnets.

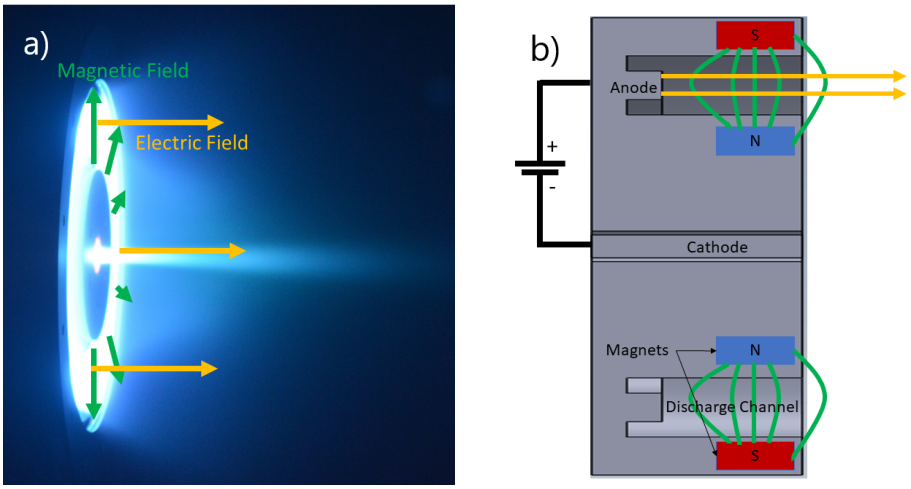

Figure 1. a) Operating Hall thruster and b) cross-sectional schematic of Hall thruster illustrating principle of operation.

To run the thruster, a potential difference is first created between the anode and cathode via a power supply. The cathode is then ignited to emit electrons that are attracted to the anode by the potential difference. As the electrons enter the thruster discharge channel, they encounter the magnetic and electric fields which form an E $\times$ B drift in the azimuthal direction. This drift impedes the electron motion towards the anode. The trapped electron population creates a sharply peaked electric field, which in turn heats the electrons through Ohmic heating. Meanwhile, a neutral gas, typically a noble gas such as xenon or krypton, is flowed through the anode down the discharge channel. When this gas encounters the warm electron population, it is ionized by electron impact collisions. The ions are rapidly accelerated by the electric field, producing thrust while these collisions with heavy species permit the electrons to cross magnetic field lines

and eventually reach the anode. The electrons stripped from the neutral particles replenish the drifting electron population while the continuous stream of electrons emitted from the cathode follows the ion beam to maintain quasi-neutrality in the thruster plume. In sum, while the ions serve to generate thrust, thruster operation is driven by the electron dynamics, which makes capturing the electron transport paramount for accurately modeling these devices.

B. Momentum Transport Model

In Hall thruster electron fluid models, the electron momentum transport is typically described by a modified form of the generalized Ohm's law.[21,26,31,34] This formulation allows for conservation of electron momentum without the need to explicitly evaluate a momentum flux or resolve the fast timescales of electron transport which significantly reduces computational expense and complexity. To arrive at the typical Ohm's law used in Hall thruster models, we consider the electron momentum equation where we assume that pressure is isotropic and electron inertia and viscous effects are negligible

$$\vec{R}_e = e\vec{j}_e \times \vec{B} + e^2 n_e \left(\vec{E} + \frac{\nabla p_e}{e n_e} - \frac{m_e \nu_{ei}}{e^4 n_e} \frac{\Sigma_Z Z \vec{j}_{i,Z}}{\Sigma_Z n_{i,Z} Z^2} \right). \tag{1}$$

Here $\vec{R}_e$ is the resistive drag force on electrons due to collisions, e is the fundamental charge, $\vec{j}_e$ is the electron current density, $\vec{B}$ is the magnetic field, n_e is the electron number density, $\vec{E}$ is the electric field, p_e is the scalar electron pressure, m_e is the electron mass, ν_{ei} is the electron-ion collision frequency, Z is the charge state of the ion, $j_{i,Z}$ is the ion current density of charge state Z, and $n_{i,Z}$ is the ion density of charge state Z. The term on the left-hand side represents the drag force on electrons due to collisions and the electron velocity, the electric and magnetic field terms represent momentum transfer due to the Lorentz force, the electron pressure term represents momentum transfer due to spatial gradients in the electron bulk properties, and the ion current density captures the contribution of the ion velocity to the momentum transfer between electrons and ions.

Generally, the drag force is represented in terms of the electron current density and the electron collision frequency per Braginskii closure.[20] However, if only classical collisions are accounted for, the electron cross-field mobility will be under-predicted by orders of magnitude.[7,8] Therefore, the resistive force is split into a classical and anomalous term

$$\vec{R}_e = R_c + R_{an} = m_e \overline{\overline{\nu}}_{e,c} \cdot \vec{j}_e + m_e \nu_{an} j_{e,\perp} \hat{\perp}. \tag{2}$$

Here $\overline{\overline{\nu}}_{e,c}$ is a tensor that accounts for the fact that the electron collision frequency is non-isotropic in a partially magnetized plasma, ν_{an} is the non-classical collision frequency, and $\hat{\perp}$ represents the direction perpendicular to the magnetic field. It is important to note that the non-classical, hereafter referred to as "anomalous," collision frequency is generally only considered to act in the perpendicular direction. Therefore, in a general Hall thruster model, Ohm's law is given by

$$m_e \overline{\overline{\nu}}_{e,c} \cdot \vec{j}_e + m_e \nu_{an} j_{e,\perp} \hat{\perp} = e\vec{j}_e \times \vec{B} + e^2 n_e \left(\vec{E} + \frac{\nabla p_e}{e n_e} - \frac{m_e \nu_{ei}}{e^4 n_e} \frac{\Sigma_Z Z \vec{j}_{i,Z}}{\Sigma_Z n_{i,Z} Z^2} \right). \tag{3}$$

By iterating on the form of ν_{an}, the electron momentum cross-field transport can be enhanced to match experimentally observed values of thruster discharge current and ion velocity. However, quantifying ν_{an} predicatively is unsolved and the search for a predictive form is still ongoing. The form for ν_{an} used in this work will be described in Sec. IV.A.

C. Energy Transport Model

The internal electron energy equation in a fluid framework is given by[21]

$$\frac{3}{2} e n_e \frac{\partial T_e}{\partial t} + \nabla \cdot \left(\frac{5}{2} e n_e T_e \vec{v}_e + \vec{q} \right) = \vec{E} \cdot \vec{j}_e + Q - \frac{3}{2} T_e \nabla \cdot \vec{j}_e, \tag{4}$$

where T_e is the electron temperature, $\vec{q}$ is the heat flux, and Q is a body heating term. Physically, the first term on the left-hand side represents the time rate of change; the divergence term contains bulk flow

"convective" and heat flux "conductive" transfer; the first term on the right is Ohmic heating; Q represents energy transfer due to body heating; and the final term on the right-hand side represents losses due to high-energy electrons convecting energy faster than the mean velocity.

Historically, there are two ways that anomalous transport is factored into the electron energy equation in Hall thruster modeling. The first is the increased Ohmic heating due to higher cross-field mobility.[17] This effect arises due to the growth of the electron current density from larger cross-field transport. This heightened current density will then enlarge the Ohmic heating, meaning we can split the Ohmic heating into a classical and anomalous term:

$$\vec{E} \cdot \vec{j}_e = \left(\vec{E} \cdot \vec{j}_e\right)_c + \left(\vec{E} \cdot \vec{j}_e\right)_{an}. \tag{5}$$

We note here this anomalous heating term is inherently coupled to the value of the anomalous collision frequency and cannot be adjusted independently of the momentum transport.

The second way in which the energy equation has been modified in the past to account for anomalous effects is through the heat flux:

$$\vec{q} = \vec{q}_c + \vec{q}_{an}, \tag{6}$$

where $\vec{q}_c, \vec{q}_{an}$ denote the classical and anomalous contributions respectively. For the classical term, we have a Fourier law based on traditional Brangiskii closure[20]:

$$\vec{q}_c = -\kappa \nabla T_e \tag{7}$$

Here κ denotes the thermal conductivity tensor, which in the partially-magnetized plasma of the Hall thruster has both perpendicular and parallel components:

$$\kappa_\parallel = a(Z^*)\frac{n_e T_e}{m_e \overline{\overline{\nu}}_\parallel} \qquad \kappa_\perp = b(Z^*)\frac{n_e T_e \overline{\overline{\nu}}_\perp}{m_e \omega_{ce}^2}, \tag{8}$$

where ν refers to the classical electron collision frequency and a and b are coefficients tabulated as a function of effective charge state Z* in Ref. 20.

For the non-classical term in Eq. 6, it is common in Hall thruster models[21,26,31,34] to adopt a term that allows for cross-field heat flux and has similar scaling to the classical Fourier law (c.f. 35):

$$\vec{q}_{an} = -b(Z^*)\frac{n_e T_e \nu_{an}}{m_e \omega_{ce}^2} \nabla T_e \hat{\perp}. \tag{9}$$

In effect, employing this result is equivalent to assuming that the effective anomalous collision frequency acts as an inter-species collision frequency in the determination of perpendicular heat flux. While this type of substitution is expedient and intuitive, first-principles underpinnings for this representation of non-classical heat flux are not well-founded. Indeed, the canonical method for arriving at this Fourier law is to assume the transport is driven by an electron-ion Coulombic, Fokker-Planck collision operator.[20] However, several of the proposed mechanisms for anomalous transport do not have this effective form. Notably, there is an emerging consensus that wave-driven effects are a key driver for momentum transfer.[36–39] The way these waves exchange momentum with the electrons has not been shown to be equivalent to an effective Fokker-Planck collision operator, thus calling into question the simplified representation shown in Eq. 9. With this in mind, when specifying the anomalous effects on the energy transport in Sec. IV, we focus on this contribution, $\vec{q}_{an}$, and its influence on the fluid predictions for the thruster dynamics.

D. Boundary Conditions

While the above sections describe the governing equations for electron transport, solving the equations requires specification of the boundary conditions. For the electron transport, the key quantities that need to be specified at the boundaries are the electron current density flux $\vec{j}_e \cdot \hat{n}$, the electron temperature, and the electrostatic potential. In general, the heat flux should also be specified, however, most Hall thruster models set $\vec{q}_e = 0$ at all boundaries.[21,31,34] Figure 2 shows a notional computational mesh for an SPT100 Hall thruster with boundary conditions types labeled. There are four types of boundary conditions present in Hall thrusters: the axis of symmetry, the cathode, free flow boundaries, and thruster walls. Bulk quantities do not generally flux through the axis of symmetry, so all fluxes at that boundary are set to 0. For the cathode

boundary, the key quantities are typically directly specified[21,31] from either a separate cathode model[21] or experimental measurements.[40] At free flow boundaries either the value or gradient of the electron temperature and electrostatic potential is specified.[21,31,34] The electron flux is set equal to the negative ion flux[21,31,34] via invoking current conservation with ions able to freely flow out of the boundary.

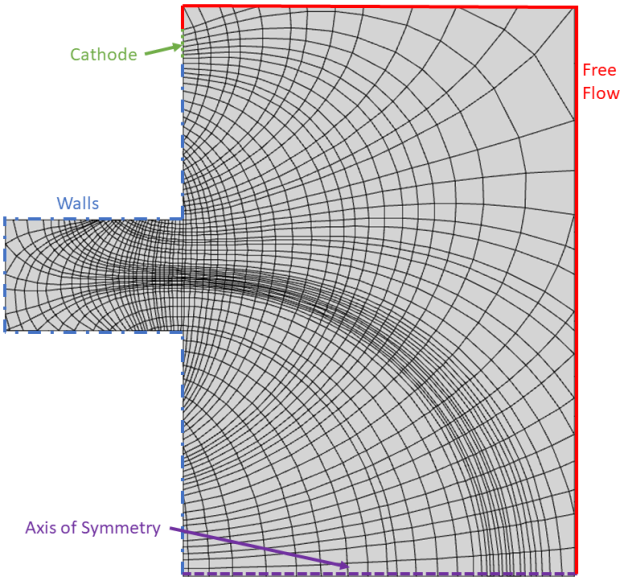

Figure 2. 2D axisymmetric computational mesh of a SPT100 Hall thruster. Notional ranges are shown for different types of boundary conditions.

The wall boundaries are handled using a sheath treatment. The exact implementation, however, varies depending on if the surface is conducting or insulating. For conducting walls, such as the anode, the electrostatic potential at the boundary is directly specified[21,31,34] which can be used to determine the potential difference between the plasma and the wall. The temperature at the walls is set to the near-wall temperature.[21,31,34] From these specifications, the electron flux is then determined by near wall electron density, electron thermal speed, and a factor based on the potential to account for the sheath repelling slow-moving electrons.[21,31,34] At insulating boundaries, current conservation is invoked to set the electron flux to the walls equal to the ion flux $\nabla \cdot \vec{j}_e = -\nabla \cdot \vec{j}_i$.[21,31,34] The ion flux to the walls is prescribed by the ion number density near the wall and the ion velocity as set by the Bohm criterion. The electron temperature is handled similarly to the conducting case in treating the electron temperature near the walls as equivalent to the electron temperature at the wall.[21,31] The potential is specified via a gradient to the wall based on the sheath criterion, which can account for secondary electron emission effects.[21,31,34] As the exact specification of the boundary condition depends on the model being utilized, we display the forms of these conditions employed in this work in Sec. III.B.

III. Hall Thruster Model

In this section, we first describe the thruster and data set used in this work. We then conclude with a description of our multi-fluid model and relevant simulation parameters.

A. Thruster and Dataset

In this work we model the H9, a 9 kW-class Hall thruster jointly developed by the University of Michigan, the Air Force Research Laboratory, and the Jet Propulsion Laboratory (JPL).[41] The H9 features a magnetically shielded topology and a center mounted cathode with a nominal operating envelope of voltages from 300 to 800 V[42] and discharge currents from 15 to 30 A.[43] For this investigation, the operating condition is a 300 V discharge voltage, 15 A discharge current, 5 μTorr background pressure, and krypton propellant. We chose this condition as measurements of the electron temperature profile, ion velocity profile, and performance metrics were all available.[33,44] Table 1 gives the values of the global performance metrics for

this operating condition. Figure 3 shows the plasma datasets for the axial component of ion velocity and electron temperature in the azimuthal direction as a function of axial position along channel centerline as a function of position downstream of the anode. Note the small error on the ion velocity curve is due to the measurement noise from Laser-Induced Fluoresce not causing significant uncertainty in the bulk velocity prediction.[45] Near the channel exit, we see an increase in the ion velocity and a locally peaked electron temperature. Both these trends indicate the presence of a strong electric field, compared to other parts of the domain, that accelerates the ions and Ohmically heats the electrons. It is worth noting that the maximum 65 eV temperature observed is higher than the previous 30-40 eV range of temperatures expected from probe measurements and numerical simulations.[43,46,47] This discrepancy is thought to be due to probes perturbing the discharge which is not present in the non-invasive measurements.[33]

Table 1. Global operating conditions for H9 operation on krypton at 300V discharge voltage and 15A discharge current[44]

Global Quantity	Value	Error
Discharge Current	15 (A)	0.1 (A)
Thrust	235.8 (mN)	2.5 (mN)
Anode Efficiency	52.2 (%)	1.1 (%)

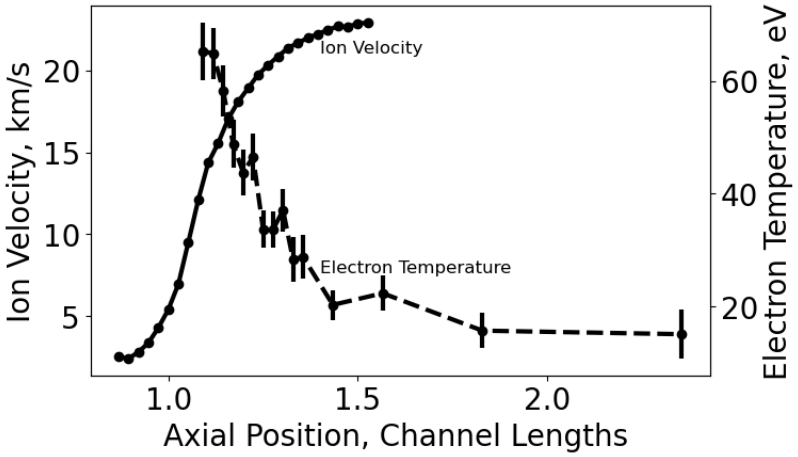

Figure 3. Experimental measurements of the axial component of ion velocity and the electron temperature in the azimuthal direction for H9 operation on krypton at 300V discharge voltage and 15A discharge current.[33] The data is plotted as a function of normalized position from the anode along channel centerline.

B. Multi-fluid Model

The multi-fluid Hall thruster model we utilize in this work is Hall2De. Hall2De is a 2D axisymmetric r-z Hall thruster code originally developed by JPL that solves for electron properties on a magnetic-field aligned mesh. An example magnetic field aligned mesh can be seen for a SPT100 Hall thruster in Fig. 2. As the formulation of the code has been extensively described elsewhere[21,48–50] we limit our description here to a high-level overview with a particular focus on the electron dynamics that we modify.

The treatment of the heavier species in the code varies between a fluid[17] and PIC[51] formulation. In this work, we use the fluid representation for heavy species. Neutrals are treated using a viewfactor representation that assumes neutral particles travel in straight-line trajectories until they are either ionized or leave the simulation domain.[48] The ions are separated into multiple fluid populations based on the electrostatic potential that the ion was born at and their charge state. Continuity, momentum, and energy equations are solved for each population. The continuity and momentum transport is solved using a semi-implicit predictor-corrector scheme[49] while the energy is solved using a forward-in-time centered-in-space representation.

In all versions of the code, electrons are represented as a fluid. The electron density is determined from the total ion density based on assuming quasi-neutrality. The electron current density is calculated from

the generalized Ohm's law given by Eq. 3. The electrostatic potential is subsequently specified from total current conversation in which ion current density and electron current density (from the generalized Ohm's law) are invoked. The electron internal energy (temperature) is described by Eq. 4. Numerically, the electron energy equation is solved with a first-order, forward-in-time, centered-in-space representation. The time rate of change, convection, and conduction terms are treated implicitly while the source terms on the right-hand side of Eq. 4 are treated explicitly. This semi-implicit formulation, along with taking substeps of the heavy species timestep when updating the electrons, allows for stable advancement of the electron properties without imposing severe timestep restrictions.

The Q term in Eq. 4 is split into elastic and inelastic contributions. Here, elastic refers to scattering collisions where energy is conserved between species tracked by the model such as Coloumb collisions. Inelastic refers to collisions where the energy is lost into unaccounted for modes such as photons emitted from electron impact excitation. The bulk heating due to elastic collisions is accounted for using a Braginksii formulation[20] that is proportional to the temperature difference between the electrons and heavy species. The energy contribution of the inelastic collisions consists of an ionization and excitation component. Ionization energy losses are computed as the product between the ionization rate and ionization energy for each ionization reaction. The excitation losses are computed as the product of an average excitation loss per ionization event and the ionization rate with the average excitation loss being a fitted function of electron temperature.[21]

As mentioned in Sec. II.D, we set the heat flux at all boundaries to 0. Therefore, we have to specify three terms at each boundary: the electron temperature, the electrostatic potential, and the flux $\vec{j}_e \cdot \hat{n}$. At the cathode boundary, the temperature and potential are specified as Dirichlet conditions and the electron flux is computed as the product of the ion number density, which is also a Dirichlet condition, and the electron thermal speed. Note that this specification treats the properties as being uniform across the cathode boundary. At free flow boundaries, the electron temperature is specified as a Dirichlet condition, the potential specified as a Neumman condition with $\nabla\phi = 0$ where ϕ is the electrostatic potential, and the electron flux set equal and opposite to the total ion flux which is formally expressed as

$$\vec{j}_e \cdot \hat{n} = -\Sigma_Z Z \vec{j}_{i,z} \cdot \hat{n}. \tag{10}$$

At conducting wall boundaries, the electron temperature is set by the temperature of the nearest cell center. The potential is specified as a Dirichlet condition with the potential drop across the sheath being the difference between this condition and the potential of the nearest cell center. Using the temperature and potential difference, the electron flux to the wall can be calculated as[21]

$$\vec{j}_e \cdot \hat{n} = j_{e,th} e^{\frac{max(\Delta\phi,0)}{T_e}}, \tag{11}$$

where $\Delta\phi = \phi - V_{wall}$ is the potential drop across the sheath and $j_{e,th} = -en_e\sqrt{\frac{eT_e}{2\pi m_e}}$ is the electron thermal flux. Physically, this expression is only valid for an electron repealing sheath ($\Delta\phi > 0$) and describes how the sheath reduces the electron flux to the walls. Additionally, the sheath modifies the average energy per electron that reaches the walls causing the total convective loss to the wall to be given by[21,52]

$$\left(\vec{j}_e T_e\right) \cdot \hat{n} = \left(\vec{j}_e \cdot \hat{n}\right)(2T_e + \Delta\phi) \tag{12}$$

where $(\vec{j}_e T_e) \cdot \hat{n}$ is the total convective electron energy loss to the walls. This expression describes the convective energy losses to the walls at conducting surfaces.

At insulating wall boundaries, the flux is specified using Eq. 10 which enforces current conservation to the walls. Like in the conducting case, the electron temperature is set by the temperature of the nearest cell center. The potential is specified as a Neumann condition with $\nabla\phi = 0$. However, the energy loss is computed similarly to the conducting boundary with modifications to account for secondary electron emission. That is, the potential drop across the sheath $\Delta\phi$ is calculated as[52]

$$\Delta\phi = T_e ln\left(\sqrt{\frac{2m_i}{\pi m_e}}(1-\gamma)\right), \tag{13}$$

where m_i is the mass of the ion and γ is the secondary electron emission coefficient. In Hall2De, γ is a fitted function of electron temperature for a given wall material with an upper limit set by to space charge

limitations.[52] The convective energy flux to the walls then becomes[21,53]

$$\left(\vec{j}_e T_e\right) \cdot \hat{n} = \left(\vec{j}_e \cdot \hat{n}\right) \left(\frac{2T_e + (1-\gamma)\Delta\phi}{1 + \frac{\gamma}{2} e^{\frac{max(\Delta\phi,0)}{T_e}} \sqrt{\frac{\pi\Delta\phi}{T_e}}} \right) \tag{14}$$

For this expression, the current density flux is still determined from Eq. 11 as in the conducting case, but the potential drop across the sheath is given by Eq. 13 rather than directly computed from the potential difference to the boundary. When there is no SEE, $\gamma = 0$, the forms of Eq. 12 (for conductors) and Eq. 14 (for insulators) agree, so Eq. 14 can be thought of as a more general form that accounts for SEE. In the thruster simulated here, the anode and pole covers are conducting while the channel walls are insulating. Modifications to these boundary conditions made in this work are further discussed in Sec. IV.

Table 2 displays the relevant baseline simulation parameters we used in this work. We used the experimental data as described in Sec. III.A to determine discharge voltage, mass flow rate, background pressure, wall material, and wall temperature. In this work, we employ six ion populations consisting of three charge states and two potential levels. The existence of three charge states is consistent with performance measurements[44,54] while two populations has been found to be sufficient to correctly describe ion behavior.[50] The discriminating potential was set to 40 V, with ions born at potentials above this level added to the main beam population and ions born at potentials below this level added to the cathode population. The cathode properties were set based on measurements of the H9 cathode.[55] The far-field electron temperature values are the average of the typical range of electron temperature in the far field plume.[21] The timestep of the heavy species was set to a fixed value of 8 ns. Finally, we found the simulation run time of 1.5 ms was sufficient for the model to converge to a steady discharge oscillation and average out any initial transient effects that may arise.

Table 2. Hall2De Simulation Parameters

Parameter	Value
Discharge Voltage	300 V
Mass Flow Rate	11.8 mg s^{-1}
Background pressure	5 μTorr
Number of ion fluids	2
Discriminating Potential	40 V
Kr charge states	0,1,2,3
Cathode flow fraction	7 %
Cathode ionization fraction	5 %
Cathode electron temperature	3.0 eV
Far field electron temperature	2.5 eV
Wall material	Boron Nitride
Wall temperature	500 °C
Heavy Species Timestep	8 ns
Simulation duration	1.5 ms

IV. Interrogating the Anomalous Energy Transport

In this section, we discuss the forms of the three anomalous transport terms we investigated in this work. We start by discussing the experimentally measured closure for the effective momentum collision frequency that we subsequently treat as "ground truth" for interrogating the energy transport. We then introduce modifications to scale the heat flux closure. Finally, we introduce a modified form of the wall boundary condition to adjust energy losses to the walls.

A. Measured Momentum Collision Frequency

In this work, we do not vary the anomalous collision frequency. Rather, we specify it using experimental measurements of the inverse electron Hall parameter, $\Omega_e^{-1} = \frac{\nu_e}{\omega_{ce}}$, which describes the ratio of the collision frequency to the cyclotron frequency.[33] Figure 4 displays the inverse Hall parameter as a function of axial distance from the anode with the measured profile being between the dotted lines. These measurements are the result of a combination of incoherent Thomson scattering measurements of the electron properties coupled with measurements of the ion velocity acceleration from laser-induced fluorescence. The data yielded by these two techniques coupled with a quasi-1D Ohm's law allowed these previous efforts to measure the anomalous collsion frequency directly and non-invasively. The profile displays the canonical shape of an anomalous transport curve with a moderate level of transport in the channel, a local minimum near the location of the peak magnetic field, and a high level of transport in the near-field plume. However, this profile does not exhibit as large of magnitude variation in the inverse Hall parameter as is typically seen in such models.[33,40,47] This departure from previous profiles is notable as the steep reduction in the local minimum is usually required to produce the steep ion acceleration observed in Hall thrusters. The implications of this departure are further discussed in Sec. VI.B.

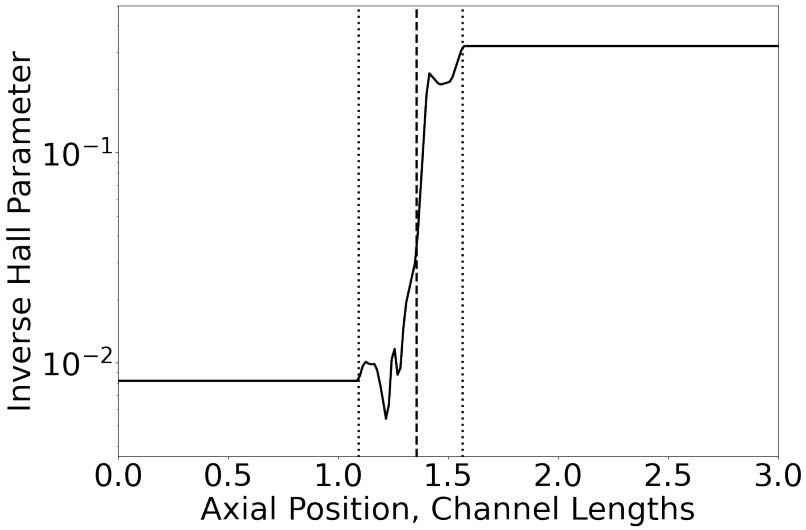

Figure 4. Experimental measurements of the inverse Hall parameter as a function of axial distance from anode along channel centerline. The dotted lines denote the bounds of experimental measurements. The data beyond is extrapolated. Data from Ref. 33. The dashed vertical line denotes the location of peak magnetic field.

If we assume that the anomalous collision frequency dominates the total electron collision frequency, which is true for most of the thruster domain,[47] these values approximately specify the ratio of the anomalous collision frequency to the cyclotron frequency. Therefore we take this profile as the ground truth value for the ratio of the anomalous collision and cyclotron frequencies, i.e. $\Omega_e^{-1} \approx \frac{\nu_{AN}}{\omega_{ce}}$.

For regions outside the dotted lines shown in Fig. 4 the experimental technique was unable to measure the profile, so we extrapolate the value of the anomalous collision frequency as a constant. The main justification for this extrapolation downstream of the experimental region is that previous numerical investigations have suggested that the non-classical inverse Hall parameter remains approximately constant downstream of the peak magnetic field. For the region upstream of the dashed lines, orders of magnitude variation in the upstream value can increase the thrust by 25%.[47] However, these studies suggest that this change does not impact the shape of the electric field in the acceleration region. Furthermore, the measured profile in Fig. 4 exhibits at most an order of magnitude variation in its local minimum, which is typically the largest variation in anomalous transport profiles. Therefore, we do not expect the assumption of constant anomalous collision frequency inside the channel to invalidate our general approach or vary by more than an order of magnitude. Finally, we note that this data is only available along centerline. Off centerline, the collision frequency is specified by scaling the centerline collision frequency along the same magnetic field line by the ratio of the

magnetic field magnitudes. Formally this scaling is expressed as

$$\nu_{an}(\beta) = \nu_{an}(\beta_{cl})\omega_{ce}(\beta_{cl}) \left(\frac{\omega_{ce}(\beta_{cl})}{\omega_{ce}(\beta)} \right)^d \tag{15}$$

where β indicates a magnetic field line, the subscript cl indicates centerline, and d is a scaling coefficient. We set d=-1 as this value was successfully utilized in previous empirical calibration of anomalous collision profiles.[47] Physically, we note that this scale is consistent with the idea that collision frequency is Bohm-like (proportional to magnetic field magnitude) along field lines.

B. Heat Flux Modification

As described in Sec. II.C, the inclusion of the anomalous collision frequency in the thermal conductivity has yet to be given a first principles justification. Therefore, as we seek to match higher than expected temperatures, a reasonable first approach is to modify the anomalous contribution to the heat flux. To do so, we introduce a scaling factor in front of the historical anomalous closure in Eq. 9 to vary its contribution

$$\vec{q}_{an} = -c_{an,\kappa} b(Z*) \frac{n_e T_e \nu_{an}}{m_e \omega_{ce}^2} \nabla T_e \hat{\perp}, \tag{16}$$

where $c_{an,\kappa}$ is a time-independent, tunable coefficient. This equation is a generalized form of the anomalous heat flux in Eq. 9, with the two forms agreeing when $c_{an,\kappa} = 1$ and the total heat flux being purely classical when $c_{an,\kappa} = 0$. Physically, a larger $c_{an,\kappa}$ will increase the heat flux resulting in more rapid diffusion of energy. This effect will then lead to flatter axial temperature profiles as the energy is spread across the domain. To keep model complexity low, we treat $c_{an,\kappa}$ as a constant throughout the computational domain. By observing the response of the electron temperature to value of the scaling coefficient, we can evaluate the extent to which it is reasonable to use the anomalous collision frequency in computing the electron heat flux.

C. Boundary Condition Modifications

As outlined in Sec. II.D, the boundary conditions are another aspect that can influence the energy transport in the thruster. Previous thermal modeling work that used Hall2De to supply estimates of plasma heat loads to the walls of a magnetically-shielded Hall thruster reduced these loads to accurately match the measured temperatures in the thruster.[56] This result suggests that Hall2De may over-predict the energy losses to the walls, making it is reasonable to scale them down. Physically, magnetic field lines in Hall thrusters are generally thought to be isothermal.[52] With isothermal field lines, the electron energy is a balance between transport across the field line and the sum of bulk heating and the wall losses at the ends of the field line.[26] Thus, diminishing the energy losses to the walls would be expected to increase the electron temperature along channel centerline and match the experimental profile.

Per Sec. III.B, Hall2De represents wall losses as a convective term $(\vec{j}_e T_e) \cdot \hat{n}$. To alter the overall losses, we scale the flux of electrons to the wall. Specifically, we introduce a factor in front of the thermal flux in Eq. 11:

$$\vec{j}_e \cdot \hat{n} = c_w j_{e,th} e^{\frac{max(\Delta\phi,0)}{T_e}}, \tag{17}$$

where c_w is a tunable coefficient. Physically, $c_w < 1$ represents fewer electrons impacting the walls than would be expected from the nominal boundary condition leading to overall lower losses. As we are adjusting the flux of electrons to the wall, c_w is applied to every wall and treated as a constant throughout the domain regardless of the wall being conducting or insulating. That is, Eq. 17 is applied to Eqs. 12 and 14 in place of Eq. 11. Note that the combination of these equations results in the scaling factor being applied to the wall losses more generally, which would also account for effects that decrease near-wall electron temperatures.

V. Results

In this section, we present trends of the model's performance metrics, ion velocity, and electron temperature as we vary the the coefficients described in Sec. IV. We first show the profiles of the model using the measured collision frequency to specify both the anomalous collision frequency and the anomalous heat flux.

We then adjust the contribution of the anomalous collision frequency to the electron heat flux to investigate its validity. Finally, we reduce the electron flux to the walls to increase the electron temperature along channel centerline.

A. Measured Collision Frequency Closure

Figure 5 displays the axial profiles of the electron temperature and ion velocity determined from the model with the anomalous collision frequency profile specified by Fig. 4. These plots have both $c_{an,\kappa}$ and c_w set to unity (i.e. the baseline approach). As can be seen for both profiles, the model does not match the experimental data within error. The peak electron temperature is approximately $\frac{3}{5}$ of the measured value while the ion acceleration towards the end of the channel is too shallow compared to the measured profile. Table 3 shows a comparison between the model and experimental global performance quantities. For the global metrics: the discharge current is under-predicted by over 2 A, the thrust is under-predicted by approximately 20 mN, and the anode efficiency matches within error. As thrust scales with discharge current,[52] it might be expected that the under-prediction in thrust would be corrected if the discharge current was closer to 15A. However, the inability of the model to capture both the local properties and discharge current while using the ground truth anomalous collision frequency suggests that the typical anomalous heat flux closure used in Hall thruster models cannot correctly capture the observed values. This result motivates adjusting the heat flux and wall loss contributions to the energy equation to better match the experimentally observed data.

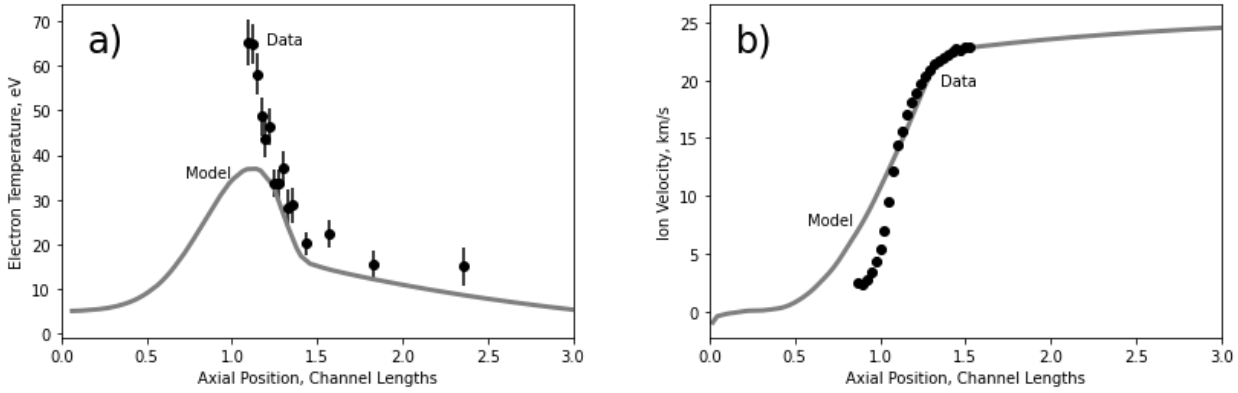

Figure 5. Comparison of experimental and model profiles of a) electron temperature and b) ion velocity along channel centerline. Model predictions are for the case of $c_{an,\kappa} = 1$ and $c_w = 1$.

Table 3. Global performance metrics for experiment and model with measured collision frequency.

Global Quantity	Experimental Value	Experimental Uncertainty	Model Value
Discharge Current	15 (A)	0.1 (A)	12.82 (A)
Thrust	235.8 (mN)	2.5 (mN)	217.21 (mN)
Anode Efficiency	52.2 (%)	1.1 %	52.0 (%)

B. Heat Flux Scaling

To examine the effect of including the anomalous collision frequency in the anomalous heat flux, Fig. 6 displays the axial profiles of the electron temperature and ion velocity along channel centerline and the global performance metrics as the $c_{an,\kappa}$ coefficient, as defined in Eq. 16, varies. Note that only the largest and smallest values of $c_{an,\kappa}$ are shown on the axial profile plots for clarity, but the intermediate values fall between the two values. Reducing the anomalous contribution to heat flux leads to higher maximum temperatures; however, it decreases the temperature on the tails of the profile. Physically, the lower heat flux prevents axial diffusion of the electron energy, which traps the energy otherwise flowing upstream and downstream of the peak temperature region. Thus, the improvement in maximum temperature comes at the

expense of the match to the experimental data greater than 1.5 channel lengths downstream. Notably, even in the case where the heat flux is purely classical, the model still under-predicts the peak electron temperature by almost 15 eV. This result suggests that it may not be possible to match the observed temperatures by tuning the cross-field heat flux alone and additional modifications to the electron energy are required.

Interestingly, the ion velocity profile in Fig. 6(b) has a sharper acceleration near the channel exit for lower values of $c_{an,\kappa}$ while the downstream match of the profiles is relatively unaffected. In other words, tuning the energy transport improved the ability of the model to correctly capture momentum transport as indicated by a steeper acceleration (stronger electric field). This trend is likely a result of the increased pressure gradient in the generalized Ohm's law. We will return to this point in Sec. VI.

For the global metrics, all values of $c_{an,\kappa}$ under-predict the discharge current by greater than 2 A, with the $c_{an,\kappa} = 0$ having a 0.2 A larger discharge current than $c_{an,\kappa}$. The thrust is under-predicted by approximately 15 mN and similar to the discharge current sees an increase with decreasing $c_{an,\kappa}$. The anode efficiency matches to within uncertainty except for $c_{an,\kappa} = 0$ suggesting that the thrust is growing faster than the discharge current. These trends are explainable by an increase in ionization rate at lower values of $c_{an,\kappa}$. As the ionization rate is driven by the electron temperature, the increase in peak electron temperature should be expected to increase the number of ions produced. The increased number of ions would then directly increase the discharge current and thrust as they are accelerated downstream. From an efficiency standpoint, higher ionization rates improve the mass efficiency which translates into an increase in anode efficiency. This trend suggests that a match in the peak electron temperature is not only critical for matching the local plasma properties but the global metrics as well.

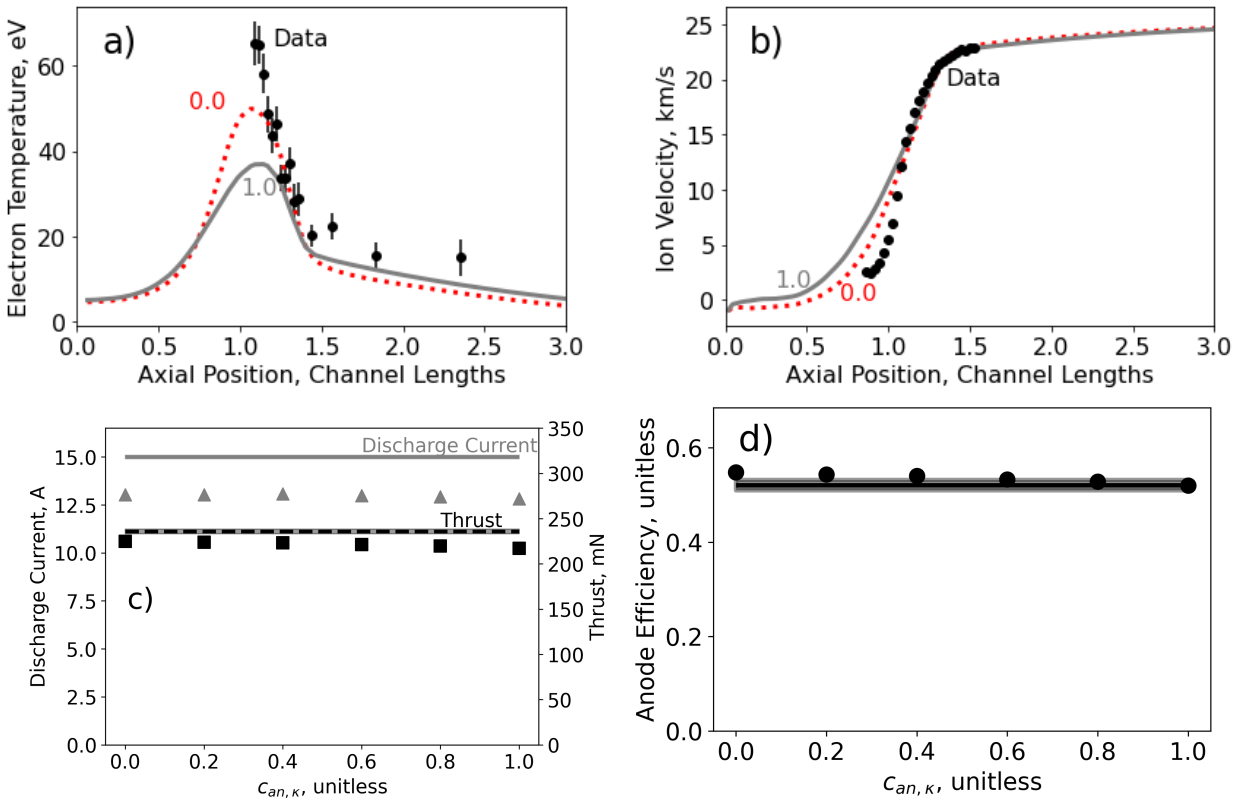

Figure 6. Comparison of experimental and model profiles along channel centerline of a) axial electron temperature and b) axial ion velocity as $c_{an,\kappa}$ is varied. Comparison of experimental and model c) discharge current and thrust, and d) anode efficiency for as $c_{an,\kappa}$ is adjusted. In c) and d) horizontal lines with shaded region represent experimental measurement and error while points represent model predictions. For all plots $c_w = 1$.

C. Wall Losses

Figure 7 displays the axial profiles and global metrics for when the wall loss coefficient c_w from Eq. 17 varies. For these plots, we set $c_{an,\kappa} = 0$, so the heat flux is purely classical. As before, the axial profiles are a subset

of coefficient values for clarity of presentation. The most notable trend in scaling c_w is that the electron temperature profiles are able to match the experimentally measured values. As c_w scales the electron flux to the walls, this result suggests that the higher than expected temperatures could potentially be attributed to an effective decrease in the electron flux toward the walls. Note that while $c_w = 0.01$ produces a peak temperature that agrees better with the measurements, the maximum temperature of $c_w = 0.1$ is within the experimental error, meaning that the preference between $c_w = 0.01$ and 0.1 should be determined by comparisons between other quantities.

For all values of c_w, the ion velocity profiles are generally the same, although $c_w = 0.1$ does provide a steeper acceleration in the latter half of the channel. The only noticeable trend is the increase in the ion velocity through the first half of the channel as c_w is reduced. This trend is likely a pressure gradient effect as increased wall losses flattens the electron temperature profile in the first half of the channel. The remaining discrepancy between the profiles is in the region near the channel exit, which will be explored further in Sec. VI. For the global metrics, however, the discharge current, thrust, and anode efficiency all increase as the wall loss decreases with the discharge current matching the experimental value for $c_w = 0.1$. Thus, while the value of $c_w = 0.01$ provides a closer match to the peak electron temperature than $c_w = 0.1$, $c_w = 0.1$ is the best-fit coefficient as it is within the measurement error of the maximum temperature and provides the best match to the global discharge current. For this condition, however, the thrust and anode efficiency are over-predicted by the model. As discussed with the $c_{an,\kappa}$ variation this trend is explainable due to the increased ionization from the higher peak temperatures. This effect and the thrust discrepancy will be further discussed in Sec.VI.

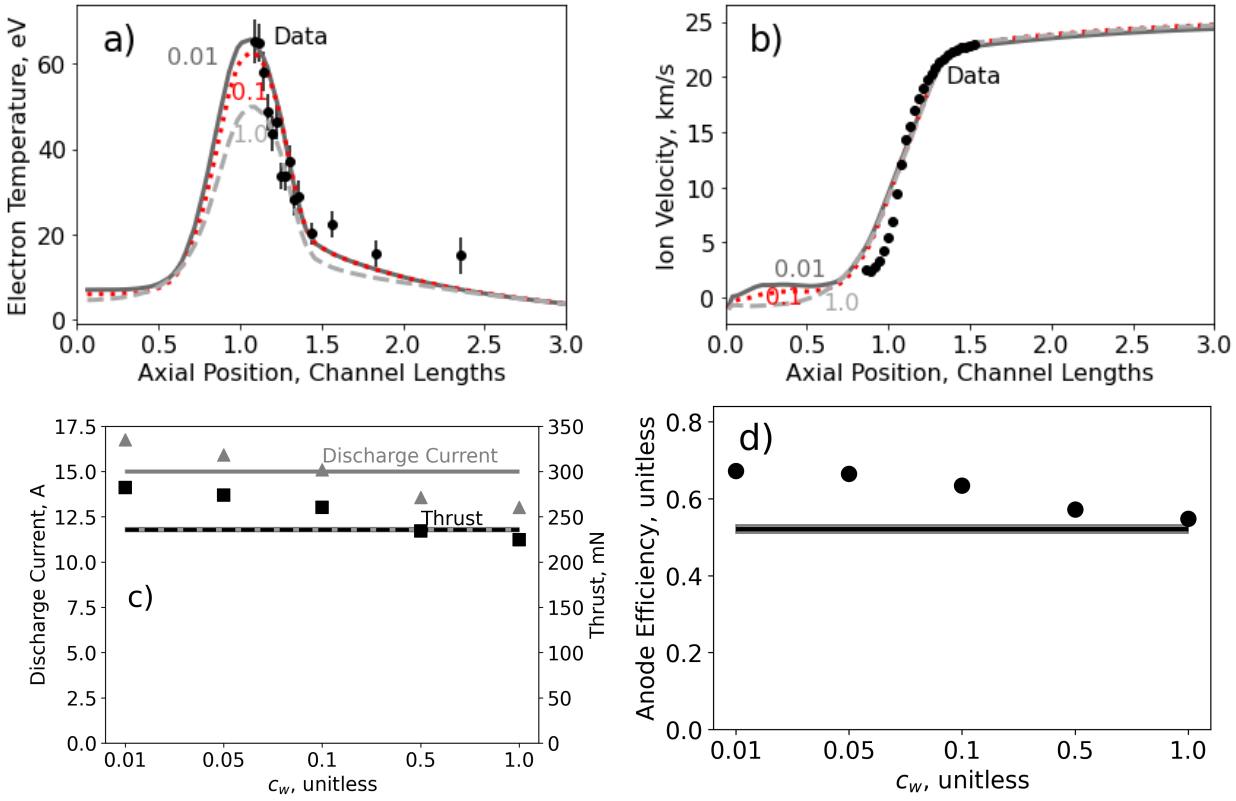

Figure 7. Comparison of experimental and model profiles along channel centerline of a) axial electron temperature and b) axial ion velocity as c_w is varied. Comparison of experimental and model c) discharge current and thrust, and d) anode efficiency for as c_w is adjusted. For all plots $c_{an,\kappa} = 0$.

To summarize, we found that including the measured anomalous collision frequency in the electron heat flux was not able to capture experimentally observed properties and metrics. Eliminating this contribution and describing the heat flux classically provided better fits to the local plasma properties and closed the gap in performance metrics but still had discrepancies larger than the experimental error. Finally, reducing the electron flux to the walls and thus the energy losses by an order of magnitude was able to match the local

plasma properties and discharge current within experimental uncertainty but over-predicted the thrust and anode efficiency. We will now discuss the implications of the classical heat flux, reduced wall losses, and remaining discrepancy between the model and experiment in detail.

VI. Discussion

In this section, we first discuss the effect of anomalous transport on the electron heat flux. We then examine how we are able to capture sharp electric fields with a transport profile that exhibits a shallower local minimum than previous work. We then consider how the heat flux and transport profile results impact the search for a predictive closure. We then provide explanations for wall loss reductions and compare them to previous work. Finally, we address the main discrepancies between the model and experimental measurements.

A. Plausibility of Heat Flux Being Classical

A key finding of this work is that it is plausible that the cross-field heat flux in the thruster may be classical. This represents a major departure, as discussed in Sec. IV.A, from conventional treatments of the heat flux in the fluid modeling of these systems. In revisiting the underlying theory of heat flux closure, however, this result may not be unexpected. Indeed, as we briefly outlined in Sec. II.C, if the key anomalous effects in the thruster are wave driven, we are not aware of a first-principles justification for why their effect on the energy transport should manifest as a modification to a Fourier law. It is possible, for example, that given the relatively collisional environment of the Hall thruster discharge, the influence of the waves on the discharge may have a negligible effect on the equilibrium shape of the electron velocity distribution function. If this is the case, then the theoretical expectation may be that the conventional Brangiskii closure holds, and only a Fourier law with classical collisions is necessary.

With that said, this interpretation is not to say that there is no impact on the heat flux, rather, that anomalous transport does not appear to play a driving role in its quantification. We note that Eq. 7 correctly quantifying the heat flux is also in contrast to previous calculations of the heat flux using the observed collision frequency which found a significant departure from the Fourier's law formulation.[57] However, as those findings used a simplified 1D model to determine the heat flux values, it is possible that 2D effects captured by our model explain this discrepancy and allow for a classical representation of the heat flux.

B. Ability to Capture Steep Electric Fields Without a Momentum Transport Barrier

Another key finding from these results is that we were able to achieve a spatially steep acceleration of the ions with a relatively relaxed prescribed anomalous collision frequency profile. For comparison, Fig. 8 plots the profile used in this work with a previously calibrated profile from Ref. 43. As can be seen in the plot, the calibrated profile requires an order of magnitude lower minimum than the measured profile to match the ion velocity profile. This result, which was remarked upon in the experimental work in Ref. 33, is notable given that previous fluid modeling work[40,47] have shown that it is typically necessary to impose a spatially-concentrated, orders of magnitude decrease in the anomalous collision frequency in the region of peak magnetic field in order to capture the steep ion acceleration.

Physically, the reason why previous modeling efforts have needed this transport barrier can be understood from the generalized Ohm's law for the perpendicular electric field. If we ignore the ion current term in Eq. 3, which is typically small in the discharge channel, we find

$$E_\perp = \frac{1+\Omega_e^2}{\sigma_\perp} j_{e,\perp} - \frac{\nabla P_e}{e n_e}, \tag{18}$$

where Ω_e is the electron Hall parameter, $\sigma_\perp$ is the conductivity perpendicular to the magnetic field, and P_e is the electron pressure. A stronger electric field will produce more rapid ion acceleration and thus steeper ion velocity profiles. As per Eq. 18, the magnitude of the electric field can be increased for a given cross-field electron current by raising the Hall parameter, i.e. implementing an effective cross-field transport barrier to the electrons.

However, Eq. 18 also shows another path toward achieving larger electric fields without a need for a rapid decrease in the anomalous collision frequency: an increased pressure gradient. A sharper pressure decline can result in stronger fields for a given Hall parameter. In our present work, we have proved this

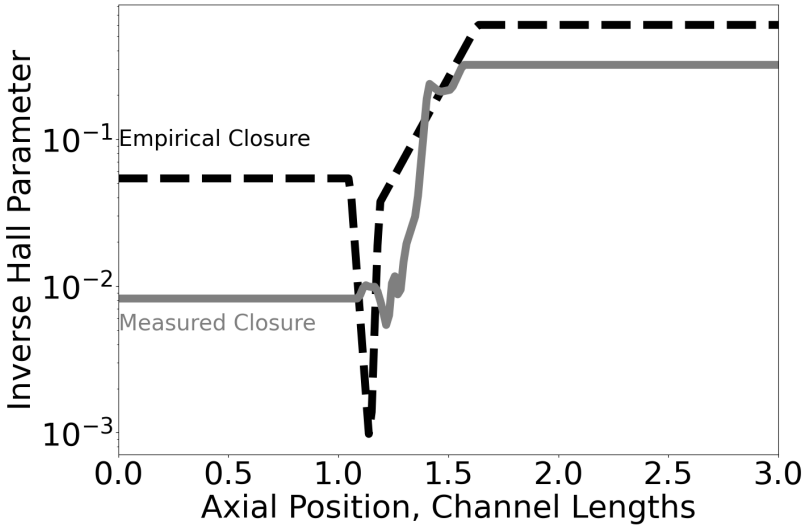

Figure 8. Inverse Hall parameter profiles from experimental measurements[33] (solid line) and from previous empirical calibration (dashed line).[43]

effect self-consistently. By effectively trapping more internal energy in the channel and thereby increasing the magnitude of the pressure gradient, we were able to achieve quantitative agreement over the majority of the ion velocity profile. This alternative pathway to capturing the ion velocity suggests that calibrating the transport profile from laser-induced fluorescence data alone is not sufficient to uniquely describe the electron dynamics.

C. Implications for closure modeling

The possibility that the conventional approach to anomalous bulk energy transport is incorrect has major potential implications for previous efforts to develop closure models for Hall effect thrusters. Indeed, as we have shown, changes to the energy equation can fundamentally alter how the model responds to a given prescribed anomalous collision frequency in the thruster. And in our particular case, we have shown that a relatively spatially relaxed profile (i.e. one that does not change by orders of magnitude, like in Fig. 4), can still lead to quantitative agreement with experimental measurements. With this in mind, many previous approaches to finding closure models for the anomalous collision frequency in these devices[15,40,58] have placed an emphasis on attempting to capture a steep transport barrier, like the empirical profile in Fig. 8, in order to capture the sharp acceleration zone in the thruster. As many of these proposed closure models in turn explicitly depend on the electron temperature,[12–16] our results suggest that these closure models may be undermined if the energy equation assumed in the models is invalid. Therefore, it may be worthwhile to revisit the self-consistent implementation of these closures after accounting for the modifications to the energy equation found in this work.

D. Possible Explanations for Reduced Electron Flux to the Walls

To match the peak electron temperatures, our results required a scaling factor value of 0.1 on the electron wall energy losses. This factor suggests that the electron flux to the walls as typically implemented in Hall thruster models is an order of magnitude too high. We will now discuss some physical reasons why we might expect reduced electron fluxes to the walls.

Within the channel, magnetically shielded Hall thrusters have a field profile shaped such that the field lines do not intersect the walls.[59] Therefore, for electrons to reach the walls they must cross magnetic field lines which we expect to reduce the electron flux to the walls. As our sheath model described in Sec. III does not account for the magnetic field, we likely over-predict the ability of the electrons to reach the walls. Numerical simulations that increased the incidence angle of the magnetic field on the channel walls and found increased electron temperatures which was directly attributed to reduced electron fluxes to the walls.[60] These

simulations confirm our suspicion that not accounting for magnetization in the sheath would lead to higher energy losses to the channel walls and lower electron temperatures.

However, at the pole surfaces, the magnetic field lines at the poles are perpendicular to the surface, so the flux of electrons into the pole is not impacted by their magnetization. Rather, we propose that the reduced flux at the walls is explainable by a magnetic mirroring effect. Generally, magnetic mirror confinement requires an increasing magnetic field strength and the adiabatic invariance of the magnetic moment.[61] As magnetic field lines converge at the poles of the thruster, the increase in field strength criterion is met as electrons follow the field lines into the poles. However, the isothermality of the field lines in this work and others means that models traditionally do not meet the adiabatic criterion for a magnetic mirror. However, 2D measurements of the electron temperature (c.f. 45) show that the electrons become superadiabatic near the poles, meeting the required conditions for a magnetic mirror effect. Therefore, it is likely that a mirroring effect not captured by the model reduces the electron flux to the poles in physical thrusters. We note that these results also show a reduced near-wall temperature that suggests lower losses are caused by a lower energy loss per electron rather than a lower flux. However, these temperatures are only 3-6 times lower than at centerline,[45] meaning a flux reduction is still necessary to fully explain the factor of 10 found in this work.

Having different physical mechanisms for reduced channel and pole fluxes is backed by the thermal modeling work on a similar thruster, which required a reduction factor to plasma wall loading of 0.52 in the channel and 0.23 on the poles.[56] Both values are higher than our best case $c_w = 0.1$, but our result is approximately within a factor of two for the pole coefficient. The discrepancy in the "pole" factor values is likely due to the fact that the thermal models used a different thruster operating at 12.5 kW than the thruster at a 4.5 kW condition used in this work. The application of the same reduction factor to all walls was done for ease of implementation. However, as seen in Fig. 7, decreasing the wall losses led to a shallower temperature gradient and increased ion velocities in the first half of the channel, suggesting that we may have dropped losses in the channel to lower than should be physically expected. This result suggests that future work should separate the flux reduction factor between channel and pole surfaces. It also suggests that the wall loss scaling results here are more applicable to the pole surfaces than in the channel, as we obtain better agreement with the pole reduction factor of Ref. 56.

E. Model Discrepancies

Here we address the remaining discrepancies between the best-case tuned model and the experimental measurements and provide physical explanations for these discrepancies.

1. Ion Velocity

Although we have found that the majority of the ion velocity profile is captured by our best-case simulation, we note that the velocity profile is still too relaxed spatially compared to experimental measurement. As mentioned in Sec. IV.A, the assumption of constant anomalous collision frequency in the channel can affect quantities such as the thrust.[47] Notably, the previous work found that the increase in the thrust was caused by the channel coefficient affecting the overlap of the ionization and acceleration regions,[47] which would affect the ion velocity profile towards the end of the channel. Therefore, future experimental and numerical work should further investigate the collision frequency inside the channel to resolve dynamics in this region.

2. Thrust

In the best-case result, the thrust was over-predicted being 10.4% larger than the experimental value. As the previous sensitivity work showed that decreasing the anomalous collision frequency in the channel could increase the measured thrust by as much as 25%,[47] our error is explainable by incorrect specification of the anomalous collision frequency in the channel. However, to reduce the thrust based on this sensitivity analysis we would need to increase the collision frequency in the channel. Per Eq. 18 this change would decrease the electric field in the channel leading to an even shallower ion acceleration when the model already predicts lower than observed ion acceleration. To simultaneously explain both discrepancies, we note that non-isothermal field lines observed in Ref. 45 would cause a pressure gradient and increase the parallel electric field. This field would accelerate ions away from channel centerline which would increase the divergence angle of the thruster. As the models presented here show isothermal field lines, it is likely

that the ion beam in the model is more collimated than in reality. Correctly capturing these 2D effects is likewise a key direction for future work to better match experimental measurements.

VII. Conclusion

In this work, we have utilized a measured anomalous collision frequency profile to investigate the energy transport in a magnetically-shielded Hall thruster operating on krypton at 300V and 15A. By describing the electron heat flux with a classical representation, we increase the peak electron temperature and provide an improved fit to the ion velocity profile. This result highlights the coupling between the resistive and pressure forces when matching electric field and ion velocity profiles. Notably, our findings suggest that the typically steep reduction in the anomalous collision frequency profiles could be due to low electron temperatures in models rather than non-classical momentum transport. The remaining discrepancy in the peak electron temperature and discharge current is resolvable by scaling down the electron energy wall losses. These results suggest that the electron flux to the walls in a thruster is an order of magnitude lower than typical fluid sheath boundary conditions suggesting the need for these boundary conditions to be re-evaluated. This finding is enforced by a number of physical reasons why the electron flux might be lower than state-of-the-art fluid models predict and qualitatively agrees with previous work that used the plasma wall loadings for thermal modeling of Hall thrusters. Finally, the remaining discrepancies in the ion velocity and thrust suggest that future experimental and numerical work should explore variations of the anomalous collision frequency in the channel and modifications to capture non-isothermal behavior along field lines. The work we have presented here demonstrates that previous treatment of the electron energy transport in Hall thrusters needs to be reconsidered. However, our results suggest that if the heat flux and boundary conditions are properly specified, predictive models of electron transport may be achievable.

Acknowledgments

This work was supported in part by a NSF GRFP, the NASA Joint Advance Propulsion Institute (80NSSC21K1118), and in part through computational resources and services provided by Advanced Research Computing at the University of Michigan.

The authors would like to thank Dr. Ioannis Mikellides and Dr. Alejandro Lopez-Ortega at the Jet Propulsion Laboratory for allowing the use of Hall2De. We would also like to thank Parker Roberts, Thomas Marks, Madison Allen, Tate Gill, William Hurley, and Miron Liu for insightful discussion and comments on the manuscript.

References

[1] Corey, R. L., Gascon, N., Delgado, J. J., Gaeta, G., Munir, S., and Lin, J. C., "Performance and Evolution of Stationary Plasma Thruster Electric Propulsion for Large Communications Satellites," 2010. URL `https://api.semanticscholar.org/CorpusID:112731706`.

[2] Levchenko, I., Bazaka, K., Ding, Y., Raitses, Y., Mazouffre, S., Henning, T., Klar, P. J., Shinohara, S., Schein, J., Garrigues, L., Kim, M., Lev, D., Taccogna, F., Boswell, R. W., Charles, C., Koizumi, H., Shen, Y., Scharlemann, C., Keidar, M., and Xu, S., "Space micropropulsion systems for Cubesats and small satellites: From proximate targets to furthermost frontiers," *Applied Physics Reviews*, Vol. 5, No. 1, 2018, p. 011104. https://doi.org/10.1063/1.5007734, URL https://doi.org/10.1063/1.5007734.

[3] Lev, D., Myers, R. M., Lemmer, K. M., Kolbeck, J., Koizumi, H., and Polzin, K., "The technological and commercial expansion of electric propulsion," *Acta Astronautica*, Vol. 159, 2019, pp. 213–227. https://doi.org/https://doi.org/10.1016/j.actaastro.2019.03.058, URL https://www.sciencedirect.com/science/article/pii/S0094576518319672.

[4] Snyder, J. S., Lopez Ortega, A., Mikellides, I. G., Li, J., Murphy, A., and Johnson, I., "Electric Propulsion for the Psyche Mission: A new trajectory and final preparations for launch," *AIAA SCITECH 2024 Forum*, Vol. AIAA 2024-1958, January 2024. https://doi.org/https://doi.org/10.2514/6.2024-1958, URL https://arc.aiaa.org/doi/10.2514/6.2024-1958.

[5] Hofer, R. R., Polk, J. E., Sekerak, M. J., Mikellides, I. G., Kamhawi, H., Sarver-Verhey, T. R., Herman, D. A., and Williams, G., "The 12.5 kW Hall Effect Rocket with Magnetic Shielding (HERMeS) for the Asteroid Redi-

rect Robotic Mission," 2016. https://doi.org/10.2514/6.2016-4825, URL https://arc.aiaa.org/doi/abs/10.2514/6.2016-4825.

[6] Taccogna, F., and Garrigues, L., "Latest progress in Hall thrusters plasma modelling," *Rev. Mod. Plasma Phys.*, Vol. 3, No. 12, 2019. https://doi.org/https://doi.org/10.1007/s41614-019-0033-1, URL https://link.springer.com/article/10.1007/s41614-019-0033-1.

[7] Fife, J. M., "Hybrid-PIC Modeling and Electrostatic Probe Survey of Hall Thruster," Ph.D. thesis, Massachusetts Institute of Technology, 1998.

[8] Morozov, A. I., and Savel'ev, V. V., *Reviews of Plasma Physics*, Vol. 21, Kluwe Academic/Plenum Publisers, 2000.

[9] Boeuf, J. P., and Garrigues, L., "Low frequency oscillations in a stationary plasma thruster," *Journal of Applied Physics*, Vol. 84, No. 7, 1998, pp. 3541–3554. https://doi.org/10.1063/1.368529, URL https://doi.org/10.1063/1.368529.

[10] Cappelli, M., Meezan, N., and Gascon, N., "Transport physics in Hall plasma thrusters," 2002. https://doi.org/10.2514/6.2002-485, URL https://arc.aiaa.org/doi/abs/10.2514/6.2002-485.

[11] Scharfe, M. K., Thomas, C. A., Scharfe, D. B., Gascon, N., Cappelli, M. A., and Fernandez, E., "Shear-Based Model for Electron Transport in Hybrid Hall Thruster Simulations," *IEEE Transactions on Plasma Science*, Vol. 36, No. 5, 2008, pp. 2058–2068. https://doi.org/10.1109/TPS.2008.2004364.

[12] Chodura, R., Bardotti, G., and Engelmann, F., "Numerical investigation of the anomalous resistivity due to two-stream instability," *Plasma Physics*, Vol. 13, No. 12, 1971, p. 1099. https://doi.org/10.1088/0032-1028/13/12/002, URL https://dx.doi.org/10.1088/0032-1028/13/12/002.

[13] Cappelli, M. A., Young, C. V., Cha, E., and Fernandez, E., "A zero-equation turbulence model for two-dimensional hybrid Hall thruster simulations," *Physics of Plasmas*, Vol. 22, No. 11, 2015, p. 114505. https://doi.org/10.1063/1.4935891, URL https://doi.org/10.1063/1.4935891.

[14] Jorns, B. A., "Two Equation Closure Model for Plasma Turbulence in a Hall Effect Thruster," *36th International Electric Propulsion Conference*, Electric Rocket Propulsion Society, Vienna, Austria, 2019. URL https://pepl.engin.umich.edu/pdf/IEPC-2019-129.pdf.

[15] Mikellides, I. G., Jorns, B., Katz, I., and Ortega, A. L., *Hall2De Simulations with a First-principles Electron Transport Model Based on the Electron Cyclotron Drift Instability*, 2016. https://doi.org/10.2514/6.2016-4618, URL https://arc.aiaa.org/doi/abs/10.2514/6.2016-4618.

[16] Lafleur, T., Baalrud, S. D., and Chabert, P., "Theory for the anomalous electron transport in Hall effect thrusters. II. Kinetic model," *Physics of Plasmas*, Vol. 23, No. 5, 2016, p. 053503. https://doi.org/10.1063/1.4948496, URL https://doi.org/10.1063/1.4948496.

[17] Marks, T. A., and Jorns, B. A., "Evaluation of algebraic models of anomalous transport in a multi-fluid Hall thruster code," *Journal of Applied Physics*, Vol. 134, No. 15, 2023, p. 153301. https://doi.org/10.1063/5.0171824, URL https://doi.org/10.1063/5.0171824.

[18] Kwon, K., "Analytical modeling of the anomalous electron collision frequency in partially magnetized E × B plasmas," *AIP Advances*, Vol. 11, No. 8, 2021, p. 085324. https://doi.org/10.1063/5.0059689, URL https://doi.org/10.1063/5.0059689.

[19] Jorns, B., "Predictive, data-driven model for the anomalous electron collision frequency in a Hall effect thruster," *Plasma Sources Science and Technology*, Vol. 27, No. 10, 2018, p. 104007. https://doi.org/10.1088/1361-6595/aae472, URL https://dx.doi.org/10.1088/1361-6595/aae472.

[20] Braginskii, S., "Transport Processes in a Plasma," *Reviews of Plasma Physics*, Vol. 1, 1965, pp. 205–311. URL https://static.ias.edu/pitp/2016/sites/pitp/files/braginskii_1965-1.pdf.

[21] Mikellides, I. G., and Katz, I., "Numerical simulations of Hall-effect plasma accelerators on a magnetic-field-aligned mesh," *Phys. Rev. E*, Vol. 86, 2012, p. 046703. https://doi.org/10.1103/PhysRevE.86.046703, URL https://link.aps.org/doi/10.1103/PhysRevE.86.046703.

[22] Morozov, A. I., and Savel'ev, V., "One-Dimensional hybrid model of a stationary plasma thruster," *Plasma Phys. Rep.*, Vol. 26, 2000, pp. 875–880.

[23] Ahedo, E., Gallardo, J. M., and Martinez-Sanchez, M., "Model of the plasma discharge in a Hall thruster with heat conduction," *Physics of Plasmas*, Vol. 9, No. 9, 2002, pp. 4061–4070. https://doi.org/10.1063/1.1499496, URL https://doi.org/10.1063/1.1499496.

[24] Hagelaar, G. J. M., Bareilles, J., Garrigues, L., and Boeuf, J. P., "Two-dimensional model of a stationary plasma thruster," *Journal of Applied Physics*, Vol. 91, No. 9, 2002, pp. 5592–5598. https://doi.org/10.1063/1.1465125, URL https://doi.org/10.1063/1.1465125.

[25] Mitchner, M., and Kruger, C. H., *Partially Ionized Gases*, John Wiley and Sons, 1973.

[26] Parra, F. I., Ahedo, E., Fife, J. M., and Martínez-Sánchez, M., "A two-dimensional hybrid model of the Hall thruster discharge," *Journal of Applied Physics*, Vol. 100, No. 2, 2006, p. 023304. https://doi.org/10.1063/1.2219165, URL https://doi.org/10.1063/1.2219165.

[27] Sahu, R., Mansour, A. R., and Hara, K., "Full fluid moment model for low temperature magnetized plasmas," *Physics of Plasmas*, Vol. 27, No. 11, 2020, p. 113505. https://doi.org/10.1063/5.0021474, URL https://doi.org/10.1063/5.0021474.

[28] Domínguez-Vázquez, A., Zhou, J., Fajardo, P., and Ahedo, E., "Analysis of the plasma discharge in a Hall Thruster vi a hybrid 2D code," *36th International Electric Propulsion Conference*, Electric Rocket Propulsion Society, Vienna, Austria, 2019.

[29] Perales-Díaz, J., Domínguez-Vázquez, A., Fajardo, P., Ahedo, E., Faraji, F., Reza, M., and Andreussi, T., "Hybrid plasma simulations of a magnetically shielded Hall thruster," *Journal of Applied Physics*, Vol. 131, No. 10, 2022, p. 103302. https://doi.org/10.1063/5.0065220, URL https://doi.org/10.1063/5.0065220.

[30] Poli, D., Bello-Benítez, E., Fajardo, P., and Ahedo, E., "Time-dependent axial fluid model of the Hall thruster discharge and its plume," *Journal of Physics D: Applied Physics*, Vol. 56, No. 41, 2023, p. 415203. https://doi.org/10.1088/1361-6463/ace2d0, URL https://dx.doi.org/10.1088/1361-6463/ace2d0.

[31] Shashkov, A., Lovtsov, A., Tomilin, D., and Kravchenko, D., "Numerical study of viscosity and heat flux role in heavy species dynamics in Hall thruster discharge," *Plasma Science and Technology*, Vol. 25, No. 1, 2022, p. 015511. https://doi.org/10.1088/2058-6272/ac82e0, URL https://dx.doi.org/10.1088/2058-6272/ac82e0.

[32] Vincent, B., Tsikata, S., and Mazouffre, S., "Incoherent Thomson scattering measurements of electron properties in a conventional and magnetically-shielded Hall thruster," *Plasma Sources Science and Technology*, Vol. 29, No. 3, 2020, p. 035015. https://doi.org/10.1088/1361-6595/ab6c42, URL https://dx.doi.org/10.1088/1361-6595/ab6c42.

[33] Roberts, P. J., and Jorns, B. A., "Laser Measurement of Anomalous Electron Diffusion in a Crossed-Field Plasma," *Phys. Rev. Lett.*, Vol. 132, 2024, p. 135301. https://doi.org/10.1103/PhysRevLett.132.135301, URL https://link.aps.org/doi/10.1103/PhysRevLett.132.135301.

[34] Domínguez-Vázquez, A., "Axisymmetric simulation codes for Hall effect thrusters and plasma plumes," Ph.D. thesis, Universidad Carlos III de Madrid, 2019.

[35] Ahedo, E., "Using electron fluid models to analyze plasma thruster discharges," *Journal of Electric Propulsion*, Vol. 2, No. 2, 2023. https://doi.org/10.1007/s44205-022-00035-6, URL https://link.springer.com/article/10.1007/s44205-022-00035-6.

[36] Tsikata, S., Lemoine, N., Pisarev, V., and Grésillon, D. M., "Dispersion relations of electron density fluctuations in a Hall thruster plasma, observed by collective light scattering," *Physics of Plasmas*, Vol. 16, No. 3, 2009, p. 033506. https://doi.org/10.1063/1.3093261, URL https://doi.org/10.1063/1.3093261.

[37] Cavalier, J., Lemoine, N., Bonhomme, G., Tsikata, S., Honoré, C., and Grésillon, D., "Hall thruster plasma fluctuations identified as the E×B electron drift instability: Modeling and fitting on experimental data," *Physics of Plasmas*, Vol. 20, No. 8, 2013, p. 082107. https://doi.org/10.1063/1.4817743, URL https://doi.org/10.1063/1.4817743.

[38] Brown, Z. A., and Jorns, B. A., "Growth and Saturation of the Electron Drift Instability in a Crossed Field Plasma," *Phys. Rev. Lett.*, Vol. 130, 2023, p. 115101. https://doi.org/10.1103/PhysRevLett.130.115101, URL https://link.aps.org/doi/10.1103/PhysRevLett.130.115101.

[39] Villafana, W., Cuenot, B., and Vermorel, O., "3D particle-in-cell study of the electron drift instability in a Hall Thruster using unstructured grids," *Physics of Plasmas*, Vol. 30, No. 3, 2023, p. 033503. https://doi.org/10.1063/5.0133963, URL https://doi.org/10.1063/5.0133963.

[40] Marks, T. A., and Jorns, B. A., "Challenges with the self-consistent implementation of closure models for anomalous electron transport in fluid simulations of Hall thrusters," *Plasma Sources Science and Technology*, Vol. 32, No. 4, 2023, p. 045016. https://doi.org/10.1088/1361-6595/accd18, URL https://dx.doi.org/10.1088/1361-6595/accd18.

[41] Hofer, R. R., Cusson, S. E., Lobbia, R. B., and Gallimore, A. D., "The H9 Magnetically Shielded Hall Thruster," *35th International Electric Propulsion Conference*, Electric Rocket Propulsion Society, Atlanta, Georgia, 2017.

[42] Cusson, S. E., Hofer, R. R., Lobbia, R. B., Jorns, B. A., and Gallimore, A. D., "Performance of the H9 Magnetically Shielded Hall Thrusters," *35th International Electric Propulsion Conference*, Electric Rocket Propulsion Society, Atlanta, Georgia, 2017.

[43] Su, L. L., Marks, T. A., and Jorns, B. A., "Trends in mass utilization of a magnetically shielded Hall thruster operating on Xenon and Krypton," *Plasma Sources Science and Technology*, 2024. https://doi.org/10.1088/1361-6595/ad52be.

[44] Su, L. L., and Jorns, B. A., "Performance comparison of a 9-kW magnetically shielded Hall thruster operating on xenon and krypton," *Journal of Applied Physics*, Vol. 130, No. 16, 2021, p. 163306. https://doi.org/10.1063/5.0066849, URL https://doi.org/10.1063/5.0066849.

[45] Roberts, P. J., Allen, M. G., and Jorns, B. A., "Thomson Scattering Investigations of Hall Thruster Anomalous Electron Transport," *38th International Electric Propulsion Conference*, Electric Rocket Propulsion Society, Toulouse, France, 2024. Paper no. 393.

[46] Hofer, R. R., Goebel, D. M., Mikellides, I. G., and Katz, I., "Magnetic shielding of a laboratory Hall thruster. II. Experiments," *Journal of Applied Physics*, Vol. 115, No. 4, 2014, p. 043304. https://doi.org/10.1063/1.4862314, URL https://doi.org/10.1063/1.4862314.

[47] Mikellides, I. G., and Ortega, A. L., "Challenges in the development and verification of first-principles models in Hall-effect thruster simulations that are based on anomalous resistivity and generalized Ohm's law*," *Plasma Sources Science and Technology*, Vol. 28, No. 1, 2019, p. 014003. https://doi.org/10.1088/1361-6595/aae63b, URL https://dx.doi.org/10.1088/1361-6595/aae63b.

[48] Katz, I., and Mikellides, I. G., "Neutral gas free molecular flow algorithm including ionization and walls for use in plasma simulations," *Journal of Computational Physics*, Vol. 230, No. 4, 2011, pp. 1454–1464. https://doi.org/https://doi.org/10.1016/j.jcp.2010.11.013, URL https://www.sciencedirect.com/science/article/pii/S0021999110006212.

[49] Ortega, A. L., and Mikellides, I. G., *A New Cell-Centered Implicit Numerical Scheme for Ions in the 2-D Axisymmetric Code Hall2De*, 2014. https://doi.org/10.2514/6.2014-3621, URL https://arc.aiaa.org/doi/abs/10.2514/6.2014-3621.

[50] Lopez Ortega, A., and Mikellides, I. G., "The importance of the cathode plume and its interactions with the ion beam in numerical simulations of Hall thrusters," *Physics of Plasmas*, Vol. 23, No. 4, 2016, p. 043515. https://doi.org/10.1063/1.4947554, URL https://doi.org/10.1063/1.4947554.

[51] Lopez Ortega, A., and Mikellides, I. G., "2D Fluid-PIC Simulations of Hall Thrusters with Self-Consistent Resolution of the Space-Charge Regions," *Plasma*, Vol. 6, No. 3, 2023, pp. 550–562. https://doi.org/10.3390/plasma6030038, URL https://www.mdpi.com/2571-6182/6/3/38.

[52] Goebel, D. M., Katz, I., and Mikellides, I. G., *Fundamentals of Electric Propulsion: Ion and Hall Thrusters*, Jet Propulsion Laboratory, 2023.

[53] Hobbs, G. D., and Wesson, J. A., "Heat flow through a Langmuir sheath in the presence of electron emission," *Plasma Physics*, Vol. 9, No. 1, 1967, p. 85. https://doi.org/10.1088/0032-1028/9/1/410, URL https://dx.doi.org/10.1088/0032-1028/9/1/410.

[54] Su, L. L., Roberts, P. J., Gill, T. M., Hurley, W. J., Marks, T. A., Sercel, C. L., Allen, M. G., Whittaker, C. B., Viges, E., and Jorns, B. A., "High-Current Density Performance of a Magnetically Shielded Hall Thruster," *Journal of Propulsion and Power*, Vol. 0, No. 0, 0, pp. 1–18. https://doi.org/10.2514/1.B39324, URL https://doi.org/10.2514/1.B39324.

[55] Georgin, M. P., Jorns, B. A., and Gallimore, A. D., "Transient non-classical transport in the hollow cathode plume I: measurements of time-varying electron collision frequency," *Plasma Sources Science and Technology*, Vol. 29, No. 10, 2020, p. 105010. https://doi.org/10.1088/1361-6595/abb0ce, URL https://dx.doi.org/10.1088/1361-6595/abb0ce.

[56] Myers, J. L., Kamhawi, H., Yim, J., and Clayman, L., *Hall Thruster Thermal Modeling and Test Data Correlation*, 2016. https://doi.org/10.2514/6.2016-4535, URL https://arc.aiaa.org/doi/abs/10.2514/6.2016-4535.

[57] Roberts, P. J., and Jorns, B., *Inferring Electron Heat Flux in a High-Power Hall Thruster with Incoherent Thomson Scattering*, 2024. https://doi.org/10.2514/6.2024-1957, URL https://arc.aiaa.org/doi/abs/10.2514/6.2024-1957.

[58] Marks, T. A., and Jorns, B., *Evaluation of several first-principles closure models for Hall thruster anomalous transport*, 2023. https://doi.org/10.2514/6.2023-0067, URL https://arc.aiaa.org/doi/abs/10.2514/6.2023-0067.

[59] Mikellides, I. G., Katz, I., Hofer, R. R., and Goebel, D. M., "Magnetic shielding of a laboratory Hall thruster. I. Theory and validation," *Journal of Applied Physics*, Vol. 115, No. 4, 2014, p. 043303. https://doi.org/10.1063/1.4862313, URL https://doi.org/10.1063/1.4862313.

[60] Keidar, M., and Beilis, I. I., "Sheath and boundary conditions for plasma simulations of a Hall thruster discharge with magnetic lenses," *Applied Physics Letters*, Vol. 94, No. 19, 2009, p. 191501. https://doi.org/10.1063/1.3132083, URL https://doi.org/10.1063/1.3132083.

[61] Chen, F. F., *Introduciton to Plasma Physics and Controlled Fusion*, Springer, 1983.